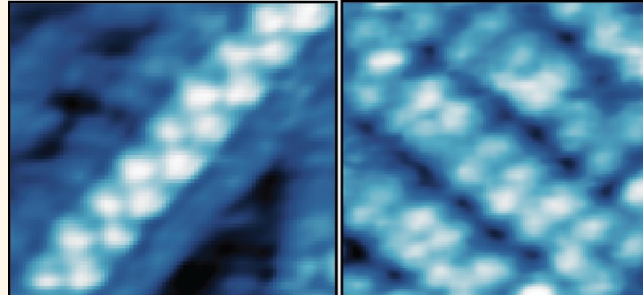


Oxygen Control of Atomic Structure and Physical Properties of SrRuO_3 Surfaces

Alexander Tselev,* P. Ganesh, Liang Qiao, Wolter Siemons, Zheng Gai, Michael D. Biegalski, Arthur P. Baddorf, and Sergei V. Kalinin

Oak Ridge National Laboratory, Oak Ridge, Tennessee 37831, United States

ABSTRACT Complex oxide thin films and heterostructures have become one of the foci for condensed matter physics research due to a broad variety of properties they exhibit. Similar to the bulk, properties of oxide surfaces can be expected to be strongly affected by oxygen stoichiometry. Here we explore the coupling between atomic structure and physical properties of SrRuO_3 (SRO), one of the most well-studied oxide materials. We perform a detailed *in situ* and *ex situ* experimental investigation of the surfaces of SRO thin films using a combination of scanning tunneling microscopy (STM), X-ray and ultraviolet photoelectron spectroscopy, SQUID magnetometry, and magnetotransport measurements, as well as *ab initio* modeling. A number of remarkable linear surface reconstructions were observed by STM and interpreted as oxygen adatoms, favorably adsorbed in a regular rectangular or zigzag patterns. The degree of oxygen coverage and different surface patterns change the work function of the thin films, and modify local electronic and magnetic properties of the topmost atomic layer. The *ab initio* modeling reveals that oxygen adatoms possess frustrated local spin moments with possible spin-glass behavior of the surface covered by adsorbed oxygen. Additionally, the modeling indicates presence of a pseudo gap on the topmost SrO layer on pristine SrO-terminated surface, suggesting possibility for realization of a surface half-metallic film.



KEYWORDS: oxide interface · oxygen adsorption · epitaxial film · surface reconstruction · *in situ* analysis · surface spin glass

Oxide thin films and heterostructures have become one of the focal points of physical research in the last two decades, with multiple examples of novel phenomena and functionalities ranging from interface orbital reconstructions, formation of unconventional 2D electron gases with coexisting superconductivity and magnetism between insulating non-magnetic materials to ferroelectric field effects and charge writing.¹ The bulk properties of oxides are strongly affected by oxygen stoichiometry, both due to changes of oxidation state of the cation, changes in molar volume due to Vegard expansion with associated changes in bond length and angles, and symmetry changes induced by vacancy ordering. Recent studies of phenomena such as charge writing for modification of the $\text{LaAlO}_3/\text{SrTiO}_3$ interface,^{2–4} tunneling in ferroelectric junction, and polarization switching in ultrathin ferroelectric

films,^{5–7} and resistive switching in ferroelectric tunnel memristors⁸ underscore the role of these phenomena on physical functionality at interfaces.

In this context, oxygen-stoichiometry-controlled properties of oxide surfaces are of special interest. Surfaces are the key intermediate active step during film growth that controls the structure and hence properties of final structures. Higher structural lability of cationic and oxygen sublattices can lead to multiple possible adatom reconstructions. Furthermore, surface electrochemistry was shown to be an essential component of phenomena such as ferroelectric phase stability or metal–insulator transitions in oxides by directly influencing physical processes in the bulk.⁹ Finally, oxygen evolution and reduction at surfaces is the key step in functionality of catalysts, solid oxide fuel cells, oxygen sensors and pumps, and multiple other energy conversion

* Address correspondence to tseleva@ornl.gov.

Received for review February 22, 2013 and accepted April 1, 2013.

Published online April 01, 2013
10.1021/nn400923n

© 2013 American Chemical Society

devices. Multiple studies have focused on exploration of oxide surfaces primarily in materials such as titanates, titania, ceria, and others that can be readily prepared by standard surface science techniques such as deposition or sputtering/annealing.^{10–15} Most of the oxide materials of interest from fundamental and applied points of view combine variable redox states of cations and a high oxygen mobility, and correspondingly, high chemical activity at the surface. Consequently, their studies require *in situ* growth and surface investigation techniques.

Here, we explore coupling between oxygen behavior and physical functionality on the surface of SrRuO_3 (SRO), a complex oxide with a perovskite structure. SRO is known for a set of properties that set it apart from most perovskites. In particular, it is a metallic conductor, exhibits itinerant ferromagnetism with a Curie temperature of 163 K in bulk, and at higher temperatures it demonstrates poor metal behavior due to electron–electron correlations.¹⁶ In the thin film form, SRO is the most widely used electrode material for oxide electronics.^{16–20} Theoretically and experimentally, it was established that SRO thin films can remain metallic down to a thickness as small as two unit cells (u.c.),^{21,22} which may be used for realization of multilayered structures with ultrathin metallic SRO layers. However, a metal–insulator transition at a thickness of 4–5 u.c. with decreasing film thickness was reported as well, still leaving the possibility and existence of such a transition a controversial issue. The physics of such a transition may be surface-related as suggested by Rondinelli *et al.*,²¹ or reminiscent of a metal–insulator transition due to oxygen octahedral rotations associated with compressive stresses as observed in thin films of a related oxide Ca_2RuO_4 .^{23,24} The origin of interfacial effects in ultrathin films grown on SRO can be strongly mediated by the nature of the surfaces of the initially grown SRO films, and understanding as well as detailed knowledge of the SRO surface, its structure and composition as functions of deposition and processing conditions are of critical importance for reliable realization of atomically defined interfaces of SRO with other complex oxides. The surface oxygen behavior is also of importance for understanding the redox chemistry of ruthenates; while a significant number of theoretical studies have been carried out to understand the electronic properties of oxide interfaces, very little has been done to understand the surface reconstructions of bare SRO surfaces and their dependence on film growth conditions.

In this work, using *in situ* scanning tunneling microscopy (STM) and photoemission spectroscopy (PES), we investigate oxygen-related surface reconstructions on a few nanometer thick films of SRO epitaxially grown by pulsed laser deposition (PLD) on (001) SrTiO_3 (STO) substrates. In a previous work, Shin *et al.*²⁵ performed atomically resolved STM of PLD-grown

SRO thin films and identified an oxygen-induced surface reconstruction, which was demonstrated to have direct influence in the sharpness of the interface between SRO and a top BaTiO_3 layer. However, STM with atomic resolution was achieved only after a prolonged 90 min postgrowth anneal of the films in oxygen atmosphere at 450 °C and a relatively high pressure of 1 Torr, which is an unusual processing step. In contrast, in this work, we have for the first time succeeded in atomic resolution imaging of as-deposited films grown at conditions that are normally used for deposition of SRO electrode layers in complex oxide functional heterostructures. The results revealed new patterns on the film surface, which were not observed before. The patterns have a linear structure and cannot be identified as reconstructions of bare SrO - or RuO_2 -terminated surfaces. Two types of linear structures—zigzag and rectangular—were observed. Using modeling based on *ab initio* density functional calculations (DFT), we identify the structures as formed by adsorbed oxygen atoms. This conclusion is supported by PES measurements. DFT modeling indicates relatively large adsorption energies of oxygen in the observed surface structures suggesting stability of the structures at the deposition temperature. In addition, DFT calculations indicate half-metallicity of the oxygen-free SrO -terminated surface and predict a spin-glass behavior in the adsorbed oxygen layer due to random ferromagnetic/antiferromagnetic coupling between spins of oxygen adatoms and spins of the underlying SRO.

RESULTS AND DISCUSSION

SRO films were grown as described in the Methods section on undoped TiO_2 -terminated (001)STO substrates with well-defined surface steps. After film growth, the samples were either annealed at deposition conditions for 15 min and then cooled down, or cooled down immediately after deposition. After cooling, the growth chamber was evacuated and the films were quickly transferred without exposure to air into an SPM chamber for STM measurements. In the following, we discuss results obtained for three samples. Film thickness, deposition parameters, and types of the observed surface structures for these three samples are given in Table 1. Reproducibility of the surface structures was confirmed with a larger set of samples.

TABLE 1. Sample Information

sample number	thickness (u.c.)	deposition temperature (°C)	anneal time (min)	observed structure
1	23	690	no	zigzag, rectangular
2	16	690	15	rectangular
3	23	650	15	zigzag, (1 × 1)

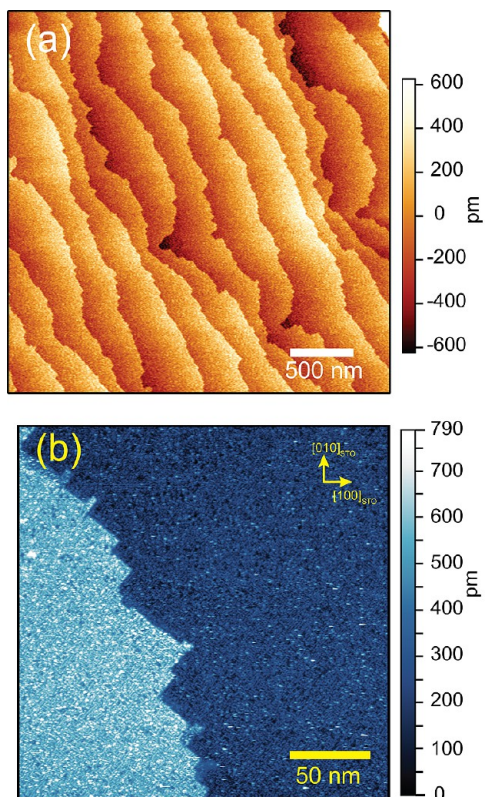


Figure 1. (a) *Ex situ* topographic AFM image and (b) low-magnification *in situ* STM image ($V_t = 2$ V, $I_t = 15$ pA) of sample 1.

Figure 1a shows an *ex situ* topographic atomic force microscopy (AFM) image of a 23 u.c.-thick SRO film deposited at a substrate temperature $T_s = 690$ °C and immediately cooled down to room temperature (sample 1 in Table 1). The AFM image and *in situ* high-pressure reflection high-energy electron diffraction (RHEED) data (Supporting Information, Figure S1) clearly indicate the step-flow growth mode for the film. Figure 1b displays an *in situ* STM image of the same film near a step edge showing an atomically smooth surface with step edges running along the $\langle 110 \rangle_{\text{pc}}$ pseudocubic directions of SRO. At this magnification scale, occasional cluster-like features are seen on the surface (larger white dots), and there are signs of the double—SrO/RuO₂—termination along the step edges. Zooming-in at a spot with traces of the double-termination reveals the double-termination clearly as seen in the STM image in the main panel of Figure 2. The line profile across the step edge (inset in the lower left corner of Figure 2) shows two steps of a 0.2 nm height, that is, half unit cell. The surface of both SrO and RuO₂-terminated portions of the film of bright spots form L-like domain patterns without ordering among domains. Importantly, the patterns are similar for both terminations (see inset in the upper right corner of Figure 2).

It is well established that in the case of SRO growth on vicinal B-terminated (TiO₂-terminated) (001)STO

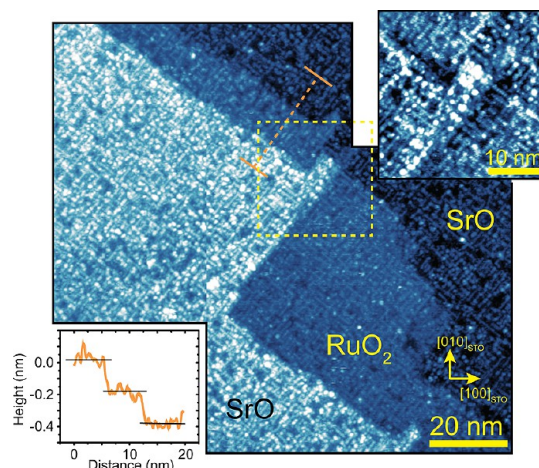


Figure 2. An STM image of a step edge with the double termination (sample 1). The inset in the upper right corner displays an STM image of the area indicated by the dashed-line in the main panel of figure. The image in the inset is made with global-plane fit to reveal structures on both terminations ($V_t = -1.6$ V, $I_t = 40$ pA). The inset in the lower left corner shows the profile along the orange line across the step edge in the main panel.

substrates, the B-terminated (RuO₂-terminated) surface of SRO is unstable due to a high oxygen activity during PLD and ready formation of volatile RuO₄, and after a few units cells, the growth takes place with the “A” surface termination.²⁶ Therefore, the surfaces of SRO films grown on (001)STO substrates are assumed to be SrO-terminated. However, in the imaged area of the film, most of the step edges showed double-termination. The observed double-termination at the step edges of the film is not associated with the possible double-termination at the step edges of the substrate (which might not be registered by AFM imaging of substrates before growth), because the step edges significantly moved during film deposition in the step-flow film growth mode. As a rule, double termination at the substrate steps results in appearance of grooves in the films because SRO does not nucleate within the A-terminated (SrO-terminated) substrate portions,^{27,28} and no such grooves are present on the surface of the sample. It is worth noting that the fact that step edges in the growing SRO films can advance with double termination has not been reported before and reveals a previously unknown aspect in the SRO film growth dynamics, showing that the RuO₂-terminated surface can be stabilized during growth, at least near the step edges. However, other samples imaged in our experiments did not show double termination at step edges in the imaged areas.

To get more insight into the structures formed on the film surface, we performed atomic-resolution imaging of the surface on both terminations. Figure 3a shows a typical high-resolution image of the pattern visible in Figure 2. The pattern consists of one-dimensional structures made up of bright spots

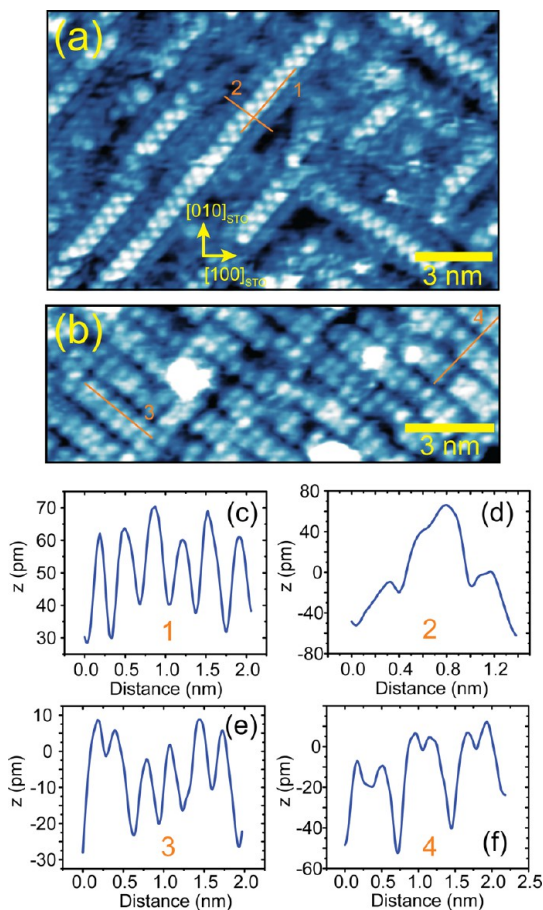


Figure 3. Higher-resolution STM images of (a) zigzag structures ($V_t = 1.4$ V, $I_t = 25$ pA) and (b) rectangular structures ($V_t = 1.6$ V, $I_t = 150$ pA); (c) profile along line 1 in panel a, along a row of the bright spots in the zigzag structure; (d) profile along line 2 in panel a, across the zigzag structure; (e) profile along line 3 in panel b, along a row in the double-row rectangular structure of the bright spots; (f) profile along line 4 in panel b, across double rows.

arranged in zigzag. The structures run along the mutually orthogonal $\langle 110 \rangle_{pc}$ pseudocubic directions of SRO. The apparent corrugation along the half-line of the structure (profile along the line 1 in Figure 3a shown in Figure 3c) is about 30 pm in amplitude. There are two lines of darker spots on both sides of the 1D zigzag structure. Therefore, the linear structures can be more accurately described as four-line with the two inner lines being elevated. The exact geometrical relations between the darker lines and in the zigzag structure could not be reliably resolved, with both zigzag and rectangular packings being likely. The line profile across such a 1D structure is shown in Figure 3d (indicated by line 2 in Figure 3a). The elevation at the peak of the structure above the bottom of the valley is about 120 ± 20 pm, which is less than half a unit cell (200 pm). The separations between neighboring spots in a line of a zigzag structure are 0.56 ± 0.04 nm, close to $\sqrt{2} \times a_{pc} \approx 0.55$ nm, where $a_{pc} = 0.393$ nm is the pseudocubic lattice constant of SRO. Separation between lines is about 0.40 ± 0.02 nm.

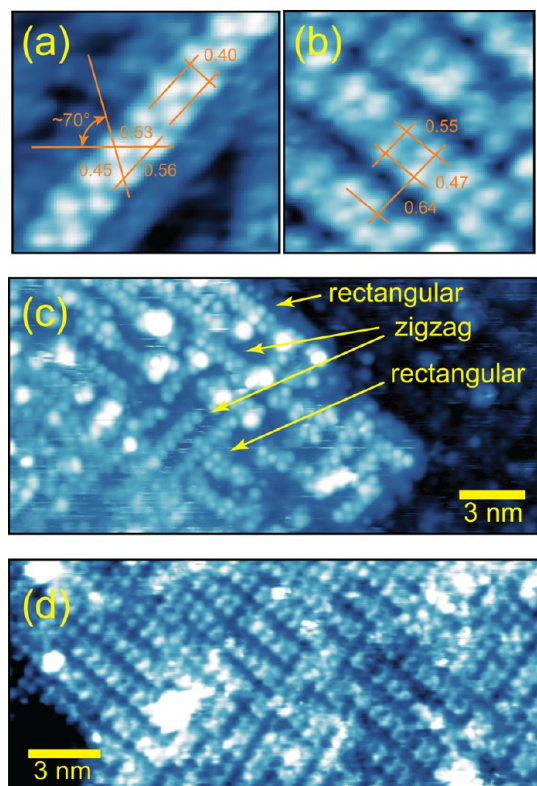


Figure 4. Characteristic dimensions of (a) zigzag and (b) rectangular structures (averages over multiple instances). The linear dimensions are shown in nanometers. (c) STM image showing simultaneous existence of rectangular and zigzag structure on the surface of sample 1 ($V_t = 1.6$ V, $I_t = 20$ pA). (d) A larger scale STM image of the surface of sample 2 (see main text, Table 1) showing the L-shaped domain pattern of the structures with rectangular packing of the bright spots ($V_t = 0.9$ V, $I_t = 60$ pA).

Other characteristic dimensions of the structure are shown in Figure 4a. The three spots in the structure equivalent to those used to indicate dimension in Figure 4a are at the vertices of a distorted equilateral triangle. The angle of the triangle opposite to the 0.56 nm side is near 70°. As evident, the separation between the bright spots is commensurate with the crystalline lattice of the films, while the separation between lines and between the nearest neighbors from different lines is not. This geometry points to a relaxation of the structure transversely to the lines, such that it requires more unit cells for the structure to repeat itself along the surface in the transverse direction. At a larger scale, sets of several parallel linear structures are intervened with similar sets running along the orthogonal direction, making altogether L-like arrangements. As was mentioned above, both SrO- and RuO₂-terminated portions of the film were covered by patterns looking identical in the STM images. An image of the RuO₂-terminated portion of the film, where the zigzag structures are clearly resolved can be found in the Supporting Information, Figure S2.

The zigzag structures are prevailing on the surface of sample 1. At the same time, on the surface this sample,

the zigzag structures alternate with similarly looking linear structures with a rectangular arrangement of the bright spots. An example of such an image is given in Figure 4c, where the zigzag and rectangular structures "compete" for the area on the SrO-terminated surface.

To explore the effect of exposure to oxygen at the deposition temperature, we have grown a 16 u.c.-thick film (sample 2 in Table 1) at the same conditions as sample 1. However, this time the film was annealed after deposition stopped for 15 min at deposition conditions, that is, at 100 mTorr oxygen pressure and $T_s = 690$ °C, before it was cooled down to room temperature. A high-resolution STM image of this sample is shown in Figure 3b. As seen, the sample surface is covered by a different pattern. We observe domains consisting of parallel double-row structures of bright spots along the $\langle 110 \rangle_{pc}$ pseudocubic directions of SRO with a rectangular atomic packing within the double-rows. Similar structures were observed among zigzag structure on the surface of sample 1. However, in the case of sample 2, only linear structures with rectangular packing of bright spots were found on the surface. Overall, this highly regular pattern can be described as a (2 × 1) reconstruction. The average distance between spots along the linear structures of this type is close to $\sqrt{2} \times 0.393$ nm ≈ 0.55 nm. The period of the structures in the transverse direction is 1.10 ± 0.05 nm with a row separation of 0.47 ± 0.02 nm within a double line (Figure 4b). Some tendency toward pairing between spots along the lines is also seen. Lower magnification STM images (Figure 4d) show that the sets of double-rows are arranged in an L-like domain pattern and noticeably more ordered than the structures on the surface of sample 1. "Antiphase" domains can be also observed, where the double-row structures running along the same direction are shifted in respect to each other by a half-period in the transverse direction (Figure 3b).

Further, we investigated influence of the deposition/annealing temperature on the surface structure. For that we have deposited a 23 u.c.-thick SRO film (sample 3 in Table 1) at a lower substrate temperature $T_s = 650$ °C and again annealed it after deposition for 15 min at deposition conditions. In this case, the intensity of the specular spot in the RHEED pattern decayed, but continuous oscillations occurred up to the very end of the deposition run, which indicated that the reduced growth mode resulted in a mixed growth mode with step flow accompanied by island formation.^{26,29} This can be attributed to insufficient diffusion time for adatoms to reach the step edges due to a reduced substrate temperature. Relatively higher substrate roughness can also contribute to this effect. *In situ* STM and *ex situ* AFM imaging showed that the film surface contains numerous pits of one-unit-cell height as a result of the mixed growth mode. However, STM images with atomic resolution

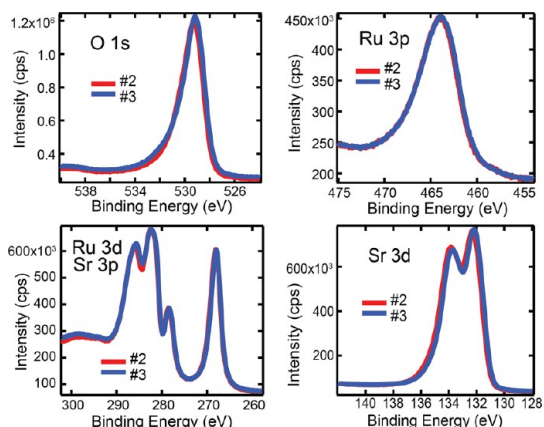


Figure 5. O 1s, Ru 3p, Ru 3d/Sr 3p, and Sr 3d core lines spectra measured with *in situ* XPS (Mg K α radiation, $h\nu = 1253.6$ eV) for samples 2 and 3.

could be obtained. They revealed that the film surface is predominantly covered by the zigzag structures similar to those found on the surface of sample 1 (Figure 3a). Additionally, areas with (1 × 1) reconstruction can be occasionally seen. The appearance of zigzag structures on the surface of the films annealed at a temperature only 40 °C below that for sample 2 suggests that the kinetics of the surface structure formation is sensitive to temperature and the rectangular structures are more likely to form at elevated T_s .

In situ X-ray photoemission spectroscopy (XPS) of core O 1s, Ru 3d, and 3p, and Sr 3p and 3d states and ultraviolet photoemission spectroscopy (UPS) of valence band O 2p and Ru 4d states provided more information on the surface composition of the films. These measurements were performed with samples 2 and 3. The samples with different patterns showed relatively small differences in their respective XPS spectra as seen in Figure 5. All core lines could be identified as originating from the SRO lattice with minor distortions, in contrast to, for example, results of references³⁰ and ³¹ where spectra were obtained from samples exposed to air (also note that the Ru peak overlaps with the C peak, precluding detailed analysis after contamination by ambient exposure). In particular, the Ru 3d peaks were found to be nearly identical for the two films. In the sample with the rectangular pattern (sample 2), the Sr 3d peaks doublet is shifted about 0.2 eV to higher binding energy in comparison with the sample 3 spectrum, suggesting that the surface of sample 2 is more oxidized, which can be interpreted as a larger oxygen coverage of the SrO-terminated surface. At the same time, the O 1s peak from sample 2 was found to have a smaller tail to higher binding energy evidencing a more uniform oxygen bonding than in the sample with the zigzag patterns.

In contrast to the XPS spectra, UPS spectra (Figure 6) of the two samples look substantially different. We note that due to lower energy of photoelectrons

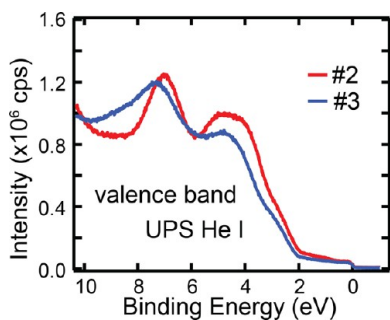


Figure 6. Valence band UPS (He-I radiation, $h\nu = 21.2$ eV) spectra of samples 2 and 3.

emitted by ultraviolet in comparison with X-ray photons, UPS is more surface sensitive. Additionally, the lower energies of UPS photons result in significantly different photoionization cross sections for valence O 2p and Ru 4d states.³² Further, as known for PLD films, the Ru 4d peak is suppressed due to Ru deficiency and associated disorder.³³ Therefore, the O 2p-related valence band peaks near 5 and 7 eV dominate the UPS spectra in comparison with the Ru 4d peak, which is closer to the Fermi energy and appears in XPS. As a result, the UPS spectra are mostly sensitive to oxygen states on the surface. In this connection, we note that the O 2p peaks of sample 2 are narrower suggesting that oxygen atoms on the surface of sample 2 are more ordered, in full accord with the STM results. The origin of the shift of the peaks toward the Fermi level in sample 2 compared to sample 3 is most probably associated with a difference in oxygen atom packing on the surface. Furthermore, the work functions of sample 2, determined by UPS onset, was found to be 0.19 eV larger than that of sample 3, again suggesting a more oxidized surface based on the trend observed in ref 34.

To assess the crystalline quality of the entire SRO films, we used *ex situ* magnetic and magnetotransport measurements. Magnetization curves of the films obtained with a Quantum Design superconducting quantum interference device (SQUID) magnetometer showed that the Curie temperatures of the films are between 135 and 140 K (see the inset in Figure 7a for results of the measurements). The values for T_c lower than the bulk value of 160 K are expected as a result of epitaxial strain in the thin films.^{22,35} Measurement of electrical resistance *versus* temperature in a zero magnetic field resulted in residual resistance ratios of about 5 (Figure 7a), which indicates a good crystalline quality of the films. (Values between 3 and 6 were reported in literature for films of comparable thickness, <10 nm.^{22,36–38}) Further, our films demonstrated a large anisotropic magnetoresistance (AMR) as displayed in Figure 7b for sample 1. As follows from the analysis of AMR data for similar films performed by Ziese *et al.*,³⁷ our film lattice structure is monoclinically distorted as expected for the films of this relatively

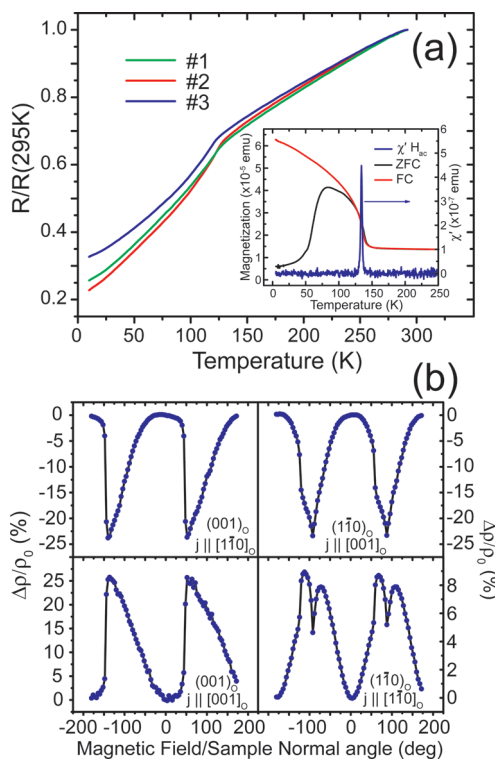


Figure 7. (a) Resistance normalized to the resistance at room temperature for samples 1, 2, and 3 as a function of temperature (see figure legend for sample-curve identification). (Inset) The dc and ac magnetizations as functions of temperature for sample 2. The dc measurements were performed in an external field of 1000 Oe. The ac field used in the measurement was 1 Oe with a frequency of 10 Hz under zero dc field. The transition temperature obtained from the ac curve is 135 K. (b) AMR curves measured at temperature $T = 10$ K in a magnetic field $H = 12$ T for sample 1. In this particular case, the AMR behavior with pronounced in-plane anisotropy corresponds to a relatively small degree of twinning in the film, which correlates with well-defined step edge orientation on the SrTiO_3 substrate surface. The crystallographic notation is shown in respect to the orthorhombic lattice of SrRuO_3 , and the mutual orientation of current and crystallographic directions was identified according to ref 37.

small thickness, and the films are twinned; the degree of twinning varies from film to film in correlation with the orientation of step edges on the substrate surface.³⁹ However, the twinning in the interior of the film should not influence the formation of the observed surface structures because the local symmetry of the linear surface structures is compatible with any of the twin domain in the bulk. Overall, these measurements indicated that our SRO films are of good crystalline quality expected for the films in the corresponding thickness range, and further, we proceed to the interpretation of our STM images.

An important observation from the experimental STM images is that similar L-shaped domain arrangements of 1D structures are present both on A- and B-terminated surfaces. This indicates that the structures have a common, nontermination-specific, origin and are not reconstructions of clean, abrupt A- and B-terminated surfaces. We note that the observed

linear structures are reminiscent of nanostructures reported to form on sputtered and annealed (001) surfaces of SrTiO_3 .^{10,40} However, the linear structures on STO have different dimensions and orientation, and cannot explain the structures observed on the surface of SRO films.

To identify the nature of the differently reconstructed surfaces, we performed density functional theory based first-principles modeling of epitaxially strained SRO thin films. Because SRO is a weakly correlated metal,²¹ with local density approximation failing to accurately reproduce spectroscopic results, here we used a spin-polarized semilocal Perdew–Burke–Ernzerhof generalized-gradient approximation (PBE-GGA)⁴¹ exchange-correlation functional within the projector augmented-wave (PAW) formalism.^{42,43} Further details of the modeling approach are described in the Methods section.

The similarity of the zigzag and rectangular patterns found both on SrO- and RuO_2 -terminated surfaces suggest that oxygen defects are at the root of these surface structures. It is possible to either create oxygen vacancies or adsorb oxygen in regular zigzag or rectangular patterns. The energy cost for formation of a single oxygen vacancy was found to be as high as 7.98 eV for an SrO-terminated surface. A Sr-vacancy can lead to underbonded oxygen atoms. Sr vacancies were also found to be energetically costly by as much as 7.19 eV. This can be understood given that Sr is fully ionic in SRO, with a strong binding energy of Sr–O ionic bond of 6.65 eV. On the other hand, the calculations showed that a single oxygen adatom adsorbs energetically favorably on an SrO-terminated surface midway between the SrO oxygen atoms with a 4.64 eV binding energy. On a RuO_2 -terminated surface, O-adatoms adsorb on top of Ru atoms with an even stronger binding energy of 5.84 eV per atom. Given the favorable energetics of oxygen adsorption on both the surface terminations and the fact that the film growth takes place in a relatively high 100 mTorr O_2 pressure, we conclude that the zigzag and rectangular patterns are formed by adsorbed oxygen adatoms.

To further explore the stability of zigzag and rectangular patterns formed by oxygen adatoms and the features in the STM images, we first freeze the zigzag and rectangular patterns on the more predominant SrO-terminated surface, as shown in Figure 8, and calculate formation energies of the patterns. The calculated energy gain of creating these patterns is 4.15 eV per oxygen adatom for the zigzag pattern and 4.37 eV per oxygen adatom for the rectangular pattern. We note that the calculated formation energies are sufficiently high for stability of the observed structures at temperatures as high as the substrate temperature in PLD, and therefore, the structures can further influence formation of the functional layers deposited on top of SRO. In the zigzag pattern,

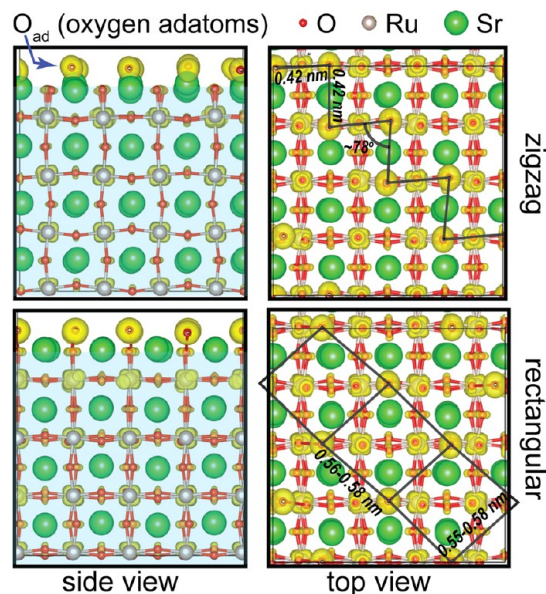


Figure 8. DFT calculated atomic arrangements corresponding to zigzag and rectangular patterns of oxygen adatoms. Yellow color shows charge density isosurfaces derived from electron states within 1.5 eV of the Fermi level.

the near-neighbor distances between oxygen adatoms in the model are ~ 0.42 nm, and the indicated angle is predominantly $\sim 76^\circ$, in reasonable agreement with the experimentally obtained 70 ± 4 degrees. The average height of the adsorbed oxygen adatom is ~ 0.14 nm above the SrO layer, in good agreement with the experimental 0.11 ± 0.03 nm. In the rectangular pattern, the oxygen nearest-neighbor distances are between 0.56 and 0.58 nm, close to 0.56 nm, as measured experimentally. Similar oxygen patterns on a RuO_2 -terminated surface were obtained by placing oxygen adatoms on top of surface Ru atoms. The adsorption energy for the zigzag pattern was 5.7 eV/adatom and for the square pattern, it was 6.0 eV/adatom, which is noticeably higher than for the SrO-terminated surface. Figure 8 also shows charge density isosurfaces derived from electron states within 1.5 eV of the Fermi level (an isosurface corresponds to a value $0.005 \text{ e}^-/\text{\AA}^3$). These states likely contributed most to the STM images at the tip bias voltages used in the STM experiments.⁴⁴ We note here that no noticeable changes in the contrast of the images were observed when changing the sign of the tip bias voltage. The contrast also did not show any significant variations with varying absolute value of the bias voltage in the range from 0.1 to 2 V (at smaller bias values, the imaging was less stable due to frequent intermittent contact between the tip and surface). As seen from calculated electronic density of states (DOS), shown in Figures S6 and S7 in the Supporting Information, adsorbed oxygen adatoms significantly contribute to the density of states in the energy range from -2 eV to $+2$ eV around the Fermi level, which again strongly indicates that they appear as the bright spots in the

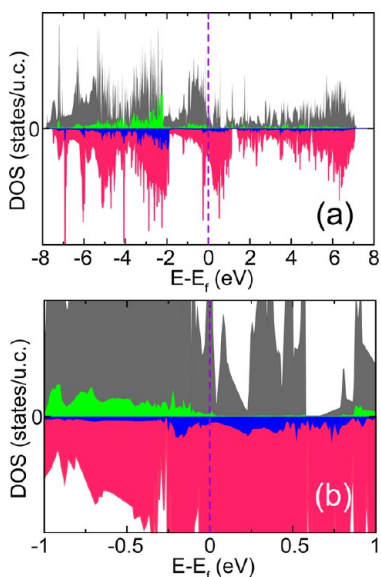


Figure 9. (a) Gray and pink: Calculated spin-resolved DOS for an SrO-terminated slab. Gray is spin-up, and pink is spin-down states. States from the surface SrO layer are also shown (with a 2-fold magnification of magnitude) in green and blue. Green is spin-up, and blue is spin-down. (b) DOS shown in panel a zoomed-in near the Fermi level to highlight a pseudogap in the majority spin states of the surface SrO layer.

STM images. Consequently, the formation of the rectangular patterns similar to that seen in Figure 4d should be interpreted as a near complete coverage of the SRO surface with adsorbed oxygen as compared to surfaces with zigzag patterns in Figure 3a, which, in turn, explained the results of PES and the difference in the work functions of samples 2 and 3. Hybridization of O p orbitals with Ru d states as seen in bulk²¹ should also lead to their significant contribution to the experimental STM images.

The presence of oxygen adatoms was also reported in related PLD-grown thin films of (001)La_{5/8}Ca_{3/8}MnO₃ on (001)STO substrates, where controlled oxygen adsorption and desorption were achieved.⁴⁵ However unlike their case, we always find our samples to be metallic both in the experiments and in modeling (see Figure 9 and Figures S4–S7 in Supporting Information for calculated DOS spectra). It is worth noting that the topmost SrO layer free of the adsorbed oxygen in the SrO-terminated slab shows a pseudogap in the majority spin channel just above the Fermi level as seen in Figure 9b, while the topmost RuO₂ layer in an RuO₂ terminated slab (Figure S5 in Supporting Information) is metallic in both the spin channels. This suggests that increasing the number of SrO layers might help to achieve surface half-metallicity in an SRO thin-film, which is of significant interest for realization of spintronic devices. The calculated magnetizations of the surface layer are 1.70 μ_B and 1.21 μ_B per Ru-atom for the SrO- and RuO₂-terminations, respectively. The lower moment on the RuO₂-terminated surface can be

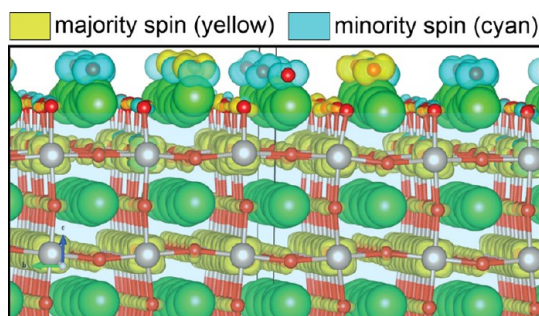


Figure 10. DFT calculated distribution of spin density among oxygen adatoms (the top line of atoms) in the rectangular structure.

attributed to the relaxation of oxygen octahedra tilting away from the orthorhombic tilts in the bulk. This indicates that the magnetic moment in SRO thin films is carried by tilted RuO₆ octahedra, and relaxation of the tilts should result in a reduction of ferromagnetic moment of the thin film. Owing to a strong hybridization of O 2p and Ru d orbitals, part of the magnetic moment of SRO appears on the oxygen site. Interestingly, the total magnetic moments in our SrO-terminated supercell slabs are 1.5 μ_B and 1.7 μ_B for the zigzag and rectangular patterns of oxygen adatoms, respectively. This is below the bulk value of 1.97 μ_B and correlates to a slightly reduced ferromagnetic transition temperature of the strained slab compared to the bulk. Interestingly, the adsorbed oxygen atoms, even on SrO-terminated surfaces, possess local moments up to 0.7 μ_B . However, the directions of the magnetic moments of individual atoms are disordered as is evident from Figure 10 showing isosurfaces of magnetization densities at 0.022 e⁻/Å³ for the rectangular pattern. This is unlike expectations for bulk-like oxygen atoms that were ferromagnetically coupled to the underlying strained SRO film. The calculated projected density of states (Figure S7 in the Supporting Information) shows that the oxygen layer is metallic unlike such surface layers being insulating in manganates,⁴⁵ but in agreement with our experimental results. A pseudogap in DOS at the Fermi level found in the model of the SrO-terminated surface suggests the possibility of decreased conductance even in the presence of the oxygen adatom layer, a topic of further detailed study. The presence of such disordered spin arrangement of surface oxygen atoms, possibly due to the weak exchange interaction with the subsurface Ru d electrons, is reminiscent of a surface spin-glass. This may further affect magnetic or charge-ordered interfaces with SRO layers.

SUMMARY AND CONCLUSIONS

We have obtained atomically resolved STM images of SrRuO₃ films grown by PLD on (001)SrTiO₃ substrates at conditions which are used for the deposition of SRO electrode layers in complex oxide functional heterostructures. Both SrO and RuO₂ surface

terminations were found in images of one of the samples, with the RuO_2 -termination covering a small fraction of the film surface along the step edges. Common to all samples, the images revealed linear—zigzag and rectangular—patterns on surfaces of the films, regardless of the type of surface termination. With use of *ab initio* modeling, the patterns were identified as adsorbed oxygen atoms, with the rectangular pattern appearing at nearly complete coverage of the film surface with adsorbed oxygen. The difference in the degree of oxygen coverage is reflected by the observed difference in the work functions of the surfaces with zigzag and rectangular patterns. The kinetics of the surface structure formation appears to be sensitive to the substrate temperature, with the rectangular pattern forming at higher temperatures with a longer exposure to oxygen. High formation energies of the observed surface patterns as found with *ab initio* calculations suggest formation and stability of the patterns at temperatures corresponding to the film deposition during PLD with possible influence

on formation of the layers deposited on top of SRO. Experimentally and analytically, the oxygen adatom layers on SRO were found metallic. DFT calculations indicate half-metallicity of the topmost SrO layer on an SrO-terminated surface free from oxygen adatoms, suggesting a way for realization of a half-metallic surface by an artificial increase of the number of SrO layers at the surface. Additionally, spin-resolved DFT calculations show a randomly oriented local spin-magnetization of adsorbed oxygen atoms suggesting spin-glass behavior of the surface covered by an oxygen layer, which may further affect properties of the functional layers deposited on SRO.

In conclusion, we have experimentally shown oxygen control of atomic structures on the surface of SRO through the growth conditions and, as indicated by *ab initio* modeling, thereby changing the surface electrostatics and magnetic properties. These are important for a complete understanding of emergent interfacial physics related to growth of other oxide thin films on SRO surfaces and for realization of novel device structures.

METHODS

Sample Preparation and Characterization. The SRO films were grown on single crystal undoped (001) SrTiO_3 substrates with miscut angles in the range between 0.07° and 0.11° (SurfaceNet, GmbH). As-delivered substrates were soaked for 45 min then sonicated for 10 min in ultrapure water at 55 °C and then etched for 30 s in a buffered oxide etch solution (pH = 4.5) at room temperature. After etch, the substrates were annealed in air at 900 °C for 4 h and then allowed to cool to room temperature at a rate less than 150 °C/h. It was found that higher anneal temperatures may result in larger surface roughness (with resulting increase in the roughness of the film due to reduced mobility of adatoms⁴⁶). After being cooled to room temperature, soaking and sonication in water were repeated as before the etching step. Soaking in water before etch and after anneal were reported as promoting the removal of SrO-termination from the STO surface.^{47,48} After that, the substrates were inspected with AFM in tapping mode using fresh, uncoated Si tips. Only substrates free of traces of SrO termination and with surface roughness root-mean-square (RMS) less than 70 pm were selected for the experiments.

To provide current path from the SRO films to the ground source for STM imaging, contact pads were deposited along edges of the substrates with room-temperature PLD in vacuum using the same SRO target as for deposition of the films. The middle part of the substrate was covered by a shadow mask during contact pad deposition.

SrRuO_3 films were deposited with PLD using a KrF laser with a 248 nm radiation wavelength and a stoichiometric SrRuO_3 ceramic target. The background pressure in the deposition chamber was less than 2×10^{-8} Torr. The depositions were performed in an oxygen atmosphere at $P_{\text{O}_2} = 100$ mTorr. The laser repetition rate was 10 Hz, and resulting growth rate was about 2.9 u.c./min. The film surface morphology during growth was monitored with *in situ* high-pressure RHEED. After growth, cooling was performed in 30 mTorr O_2 down to a temperature of ~ 200 °C. After that, the growth chamber was evacuated and the films were quickly transferred without exposure to air into an SPM chamber with a base pressure less than 2×10^{-10} Torr. The STM images were taken in the constant current mode at room temperature with an Omicron VT SPM using commercial Pt–Ir tips (Agilent Technologies). The bias was applied to the tip and the sample was grounded. After STM imaging, XPS and UPS

analyses were performed without breaking vacuum at a pressure of $\sim 2 \times 10^{-10}$ Torr. Topographic AFM imaging and magnetic and transport measurements were made *ex situ* after taking samples to air.

DFT Calculations. A PBE-GGA functional was used both with and without spin-polarization within the PAW formalism implemented in the Vienna *ab-Initio* Simulation Package (VASP). The bulk SRO calculations were performed for the *Pbnm* structure with experimental lattice parameters, but with relaxed ionic positions. Density of states calculations in this case used a $12 \times 12 \times 10$ \mathbf{k} -point mesh and a 500 eV energy cutoff. Density of states obtained from the PBE-GGA functional (see Supporting Information, Figure S4) shows that the bulk SRO is almost a half-metal, with a magnetic moment of $1.97 \mu_{\text{B}}$ /u.c. Since the films were 16 or 23 unit-cells thick, the effect of the SRO/STO interface is only the epitaxial strain imposed on the film by the underlying STO substrate. As such, we studied strained SRO thin films with their *c* axis of the *Pbnm* structure being in-plane and constrained to the cubic STO lattice parameter of 0.3905 nm, while the film $\langle 110 \rangle$ direction is out-of-plane. To freeze surface defects running at $\sim 45^\circ$ in respect to the pseudocubic $\langle 100 \rangle_{\text{pc}}$ direction, we modeled $4 \times 4 \times 4$ slabs. The bottom two unit-cells were kept fixed while the remaining layers were relaxed. For the $4 \times 4 \times L$ slabs, where $L = 4$ for nondefect calculations, ionic relaxations were performed using a single \mathbf{k} -point, the Γ -point. The slabs were separated by at least 1 nm of vacuum to minimize their interactions. Density of states and magnetization and work function calculations for the slabs were performed using a $2 \times 2 \times 1$ \mathbf{k} -point mesh and 500 eV plane-wave cut off for the kinetic energy.

Conflict of Interest: The authors declare no competing financial interest.

Acknowledgment. The authors thank P. Kent, P. Maksymovych, M. Pan, W. Lin, and A. Belianinov for helpful suggestions and assistance. This research was sponsored by the Division of Materials Sciences and Engineering, Office of Basic Energy Sciences, U.S. Department of Energy (AT, WS, SVK). Research was conducted at the Center for Nanophase Materials Sciences which is sponsored at Oak Ridge National Laboratory by the Scientific User Facilities Division, Office of Basic Energy Sciences, U.S. Department of Energy.

Supporting Information Available: RHEED data, additional STM images, and calculated DOS spectra. This material is available free of charge via the Internet at <http://pubs.acs.org>.

REFERENCES AND NOTES

- Zubko, P.; Gargiulo, S.; Gabay, M.; Ghosez, P.; Triscone, J. M. Interface Physics in Complex Oxide Heterostructures. In *Annual Review of Condensed Matter Physics*; Langer, J. S., Ed.; 2011; Vol. 2, pp 141–165.
- Cen, C.; Thiel, S.; Hammerl, G.; Schneider, C. W.; Andersen, K. E.; Hellberg, C. S.; Mannhart, J.; Levy, J. Nanoscale Control of an Interfacial Metal-Insulator Transition at Room Temperature. *Nat. Mater.* **2008**, *7*, 298–302.
- Xie, Y.; Bell, C.; Yajima, T.; Hikita, Y.; Hwang, H. Y. Charge Writing at the $\text{LaAlO}_3/\text{SrTiO}_3$ Surface. *Nano Lett.* **2010**, *10*, 2588–2591.
- Kumar, A.; Arruda, T. M.; Kim, Y.; Ivanov, I. N.; Jesse, S.; Bark, C. W.; Bristow, N. C.; Artacho, E.; Littlewood, P. B.; Eom, C.-B.; et al. Probing Surface and Bulk Electrochemical Processes on the $\text{LaAlO}_3\text{-SrTiO}_3$ Interface. *ACS Nano* **2012**, *6*, 3841–3852.
- Garcia, V.; Fusil, S.; Bouzehouane, K.; Enouz-Vedrenne, S.; Mathur, N. D.; Barthelemy, A.; Bibes, M. Giant Tunnel Electroresistance for Non-Destructive Readout of Ferroelectric States. *Nature* **2009**, *460*, 81–84.
- Gruverman, A.; Wu, D.; Lu, H.; Wang, Y.; Jang, H. W.; Folkman, C. M.; Zhuravlev, M. Y.; Felker, D.; Rzchowski, M.; Eom, C. B.; et al. Tunneling Electroresistance Effect in Ferroelectric Tunnel Junctions at the Nanoscale. *Nano Lett.* **2009**, *9*, 3539–3543.
- Bristow, N. C.; Stengel, M.; Littlewood, P. B.; Pruneda, J. M.; Artacho, E. Electrochemical Ferroelectric Switching: Origin of Polarization Reversal in Ultrathin Films. *Phys. Rev. B* **2012**, *85*.
- Kim, D. J.; Lu, H.; Ryu, S.; Bark, C. W.; Eom, C. B.; Tsymbal, E. Y.; Gruverman, A. Ferroelectric Tunnel Memristor. *Nano Lett.* **2012**, *12*, 5697–5702.
- Kalinin, S. V.; Borisevich, A.; Fong, D. Beyond Condensed Matter Physics on the Nanoscale: The Role of Ionic and Electrochemical Phenomena in the Physical Functionalities of Oxide Materials. *ACS Nano* **2012**, *6*, 10423–10437.
- Marshall, M. S. J.; Becerra-Toledo, A. E.; Payne, D. J.; Egdell, R. G.; Marks, L. D.; Castell, M. R. Structure and Composition of Linear TiO_x Nanostructures on $\text{SrTiO}_3(001)$. *Phys. Rev. B* **2012**, *86*, 125416.
- Shimizu, R.; Iwaya, K.; Ohsawa, T.; Shiraki, S.; Hasegawa, T.; Hashizume, T.; Hitosugi, T. Atomic-Scale Visualization of Initial Growth of Homoepitaxial SrTiO_3 Thin Film on an Atomically Ordered Substrate. *ACS Nano* **2011**, *5*, 7967–7971.
- Murray, P. W.; Leibsle, F. M.; Muryn, C. A.; Fisher, H. J.; Flipse, C. F. J.; Thornton, G. Interrelationship of Structural Elements on $\text{TiO}_2(100)\text{-}(1 \times 3)$. *Phys. Rev. Lett.* **1994**, *72*, 689–692.
- Park, J. B.; Graciani, J.; Evans, J.; Stacchiola, D.; Ma, S.; Liu, P.; Nambu, A.; Sanz, J. F.; Hrbek, J.; Rodriguez, J. A. High Catalytic Activity of $\text{Au}/\text{CeO}_x/\text{TiO}_2(110)$ Controlled by the Nature of the Mixed-Metal Oxide at the Nanometer Level. *Proc. Natl. Acad. Sci.* **2009**, *106*, 4975–4980.
- Esch, F.; Fabris, S.; Zhou, L.; Montini, T.; Africh, C.; Fornasiero, P.; Comelli, G.; Rosei, R. Electron Localization Determines Defect Formation on Ceria Substrates. *Science* **2005**, *309*, 752–755.
- Bonnell, D. A.; Garra, J. Scanning Probe Microscopy of Oxide Surfaces: Atomic Structure and Properties. *Rep. Prog. Phys.* **2008**, *71*, 044501.
- Koster, G.; Klein, L.; Siemons, W.; Rijnders, G.; Dodge, J. S.; Eom, C.-B.; Blank, D. H. A.; Beasley, M. R. Structure, Physical Properties, and Applications of SrRuO_3 Thin Films. *Rev. Mod. Phys.* **2012**, *84*, 253–298.
- Ahn, C. H.; Triscone, J. M.; Mannhart, J. Electric Field Effect in Correlated Oxide Systems. *Nature* **2003**, *424*, 1015–1018.
- Junquera, J.; Ghosez, P. Critical Thickness for Ferroelectricity in Perovskite Ultrathin Films. *Nature* **2003**, *422*, 506–509.
- Takahashi, K. S.; Sawa, A.; Ishii, Y.; Akoh, H.; Kawasaki, M.; Tokura, Y. Inverse Tunnel Magnetoresistance in All-Perovskite Junctions of $\text{La}_{0.7}\text{Sr}_{0.3}\text{MnO}_3/\text{SrTiO}_3/\text{SrRuO}_3$. *Phys. Rev. B* **2003**, *67*, 094413.
- Ramesh, R.; Spaldin, N. A. Multiferroics: Progress and Prospects in Thin Films. *Nat. Mater.* **2007**, *6*, 21–29.
- Rondinelli, J. M.; Caffrey, N. M.; Sanvito, S.; Spaldin, N. A. Electronic Properties of Bulk and Thin Film SrRuO_3 : Search for the Metal-Insulator Transition. *Phys. Rev. B* **2008**, *78*, 155107.
- Chang, Y. J.; Kim, C. H.; Phark, S. H.; Kim, Y. S.; Yu, J.; Noh, T. W. Fundamental Thickness Limit of Itinerant Ferromagnetic SrRuO_3 Thin Films. *Phys. Rev. Lett.* **2009**, *103*, 057201.
- Nakamura, F.; Goko, T.; Ito, M.; Fujita, T.; Nakatsuji, S.; Fukazawa, H.; Maeno, Y.; Alireza, P.; Forsythe, D.; Julian, S. R. From Mott Insulator to Ferromagnetic Metal: A Pressure Study of Ca_2RuO_4 . *Phys. Rev. B* **2002**, *65*, 220402.
- Miao, L.; Silwal, P.; Zhou, X.; Stern, I.; Peng, J.; Zhang, W.; Spinu, L.; Mao, Z.; Kim, D. H. Itinerant Ferromagnetism and Geometrically Suppressed Metal-Insulator Transition in Epitaxial Thin Films of Ca_2RuO_4 . *Appl. Phys. Lett.* **2012**, *100*, 052401.
- Shin, J.; Borisevich, A. Y.; Meunier, V.; Zhou, J.; Plummer, E. W.; Kalinin, S. V.; Baddorf, A. P. Oxygen-Induced Surface Reconstruction of SrRuO_3 and Its Effect on the BaTiO_3 Interface. *ACS Nano* **2010**, *4*, 4190–4196.
- Rijnders, G.; Blank, D. H. A.; Choi, J.; Eom, C.-B. Enhanced Surface Diffusion through Termination Conversion During Epitaxial SrRuO_3 Growth. *Appl. Phys. Lett.* **2004**, *84*, 505–507.
- Bachelet, R.; Sánchez, F.; Santiso, J.; Munuera, C.; Ocal, C.; Fontcuberta, J. Self-Assembly of $\text{SrTiO}_3(001)$ Chemical-Terminations: A Route for Oxide-Nanostructure Fabrication by Selective Growth. *Chem. Mater.* **2009**, *21*, 2494–2498.
- Kan, D.; Shimakawa, Y. Geometric-Shape-Dependent Structural Transition Behavior in (110) SrRuO_3 Epitaxial Thin Films. *J. Appl. Phys.* **2012**, *111*, 093532.
- Hong, W.; Lee, H. N.; Yoon, M.; Christen, H. M.; Lowndes, D. H.; Suo, Z.; Zhang, Z. Persistent Step-Flow Growth of Strained Films on Vicinal Substrates. *Phys. Rev. Lett.* **2005**, *95*, 095501.
- Mlynarczyk, M.; Szot, K.; Petraru, A.; Poppe, U.; Breuer, U.; Waser, R.; Tomala, K. Surface Layer of SrRuO_3 Epitaxial Thin Films under Oxidizing and Reducing Conditions. *J. Appl. Phys.* **2007**, *101*.
- Shin, J.; Kalinin, S. V.; Lee, H. N.; Christen, H. M.; Moore, R. G.; Plummer, E. W.; Baddorf, A. P. Surface Stability of Epitaxial SrRuO_3 Films. *Surf. Sci.* **2005**, *581*, 118–132.
- Yeh, J. J.; Lindau, I. Atomic Subshell Photoionization Cross Sections and Asymmetry Parameters: $1 \leq Z \leq 103$. *Atom. Data Nuclear Data Tables* **1985**, *32*, 1–155.
- Siemons, W.; Koster, G.; Vailionis, A.; Yamamoto, H.; Blank, D. H. A.; Beasley, M. R. Dependence of the Electronic Structure of SrRuO_3 and Its Degree of Correlation on Cation Off-Stoichiometry. *Phys. Rev. B* **2007**, *76*, 075126.
- Hartmann, A. J.; Neilson, M.; Lamb, R. N.; Watanabe, K.; Scott, J. F. Ruthenium Oxide and Strontium Ruthenate Electrodes for Ferroelectric Thin-Films Capacitors. *Appl. Phys. A: Mater. Sci. Process.* **2000**, *70*, 239–242.
- Gan, Q.; Rao, R. A.; Eom, C. B.; Garrett, J. L.; Lee, M. Direct Measurement of Strain Effects on Magnetic and Electrical Properties of Epitaxial SrRuO_3 Thin Films. *Appl. Phys. Lett.* **1998**, *72*, 978–980.
- Schultz, M.; Levy, S.; Reiner, J. W.; Klein, L. Magnetic and Transport Properties of Epitaxial Films of SrRuO_3 in the Ultrathin Limit. *Phys. Rev. B* **2009**, *79*, 125444.
- Ziese, M.; Vrejou, I.; Hesse, D. Structural Symmetry and Magnetocrystalline Anisotropy of SrRuO_3 Films on SrTiO_3 . *Phys. Rev. B* **2010**, *81*, 184418.
- Genish, I.; Kats, Y.; Klein, L.; Reiner, J. W.; Beasley, M. R. Paramagnetic Anisotropic Magnetoresistance in Thin Films of SrRuO_3 . *J. Appl. Phys.* **2004**, *95*, 6681–6683.
- Vailionis, A.; Siemons, W.; Koster, G. Strain-Induced Single-Domain Growth of Epitaxial SrRuO_3 Layers on

SrTiO₃: A High-Temperature X-ray Diffraction Study. *Appl. Phys. Lett.* **2007**, *91*, 071907–3.

40. Marshall, M. S. J.; Becerra-Toledo, A. E.; Marks, L. D.; Castell, M. R. Surface and Defect Structure of Oxide Nanowires on SrTiO₃. *Phys. Rev. Lett.* **2011**, *107*, 086102.

41. Perdew, J. P.; Burke, K.; Ernzerhof, M. Generalized Gradient Approximation Made Simple. *Phys. Rev. Lett.* **1996**, *77*, 3865–3868.

42. Blöchl, P. E. Projector Augmented-Wave Method. *Phys. Rev. B* **1994**, *50*, 17953–17979.

43. Kresse, G.; Joubert, D. From Ultrasoft Pseudopotentials to the Projector Augmented-Wave Method. *Phys. Rev. B* **1999**, *59*, 1758–1775.

44. Tersoff, J.; Hamann, D. R. Theory of the Scanning Tunneling Microscope. *Phys. Rev. B* **1985**, *31*, 805–813.

45. Fuchigami, K.; Gai, Z.; Ward, T. Z.; Yin, L. F.; Snijders, P. C.; Plummer, E. W.; Shen, J. Tunable Metallicity of the La_{5/8}Ca_{3/8}MnO₃(001) Surface by an Oxygen Overlayer. *Phys. Rev. Lett.* **2009**, *102*, 066104.

46. Boscher, J. E.; Tybella, T. Qualitative Determination of Surface Roughness by *in Situ* Reflection High Energy Electron Diffraction. *Appl. Phys. Lett.* **2012**, *100*, 151604–4.

47. Koster, G.; Kropman, B. L.; Rijnders, G. J. H. M.; Blank, D. H. A.; Rogalla, H. Quasi-Ideal Strontium Titanate Crystal Surfaces through Formation of Strontium Hydroxide. *Appl. Phys. Lett.* **1998**, *73*, 2920–2922.

48. Kobayashi, D.; Kumigashira, H.; Oshima, M.; Ohnishi, T.; Lippmaa, M.; Ono, K.; Kawasaki, M.; Koinuma, H. High-Resolution Synchrotron-Radiation Photoemission Characterization for Atomically-Controlled SrTiO₃(001) Substrate Surfaces Subjected to Various Surface Treatments. *J. Appl. Phys.* **2004**, *96*, 7183–7188.